

Review

Recent Advances in Surface Plasmon Resonance Microscopy

Songfeng Huang , Jiajie Chen * , Teliang Zhang, Xiaoqi Dai, Xueliang Wang, Jianxing Zhou , Weifu Kong, Qian Liu, Junle Qu  and Yonghong Shao *

Key Laboratory of Optoelectronic Devices and Systems of Ministry of Education and Guangdong Province, College of Physics and Optoelectronic Engineering, Shenzhen University, Shenzhen 518060, China

* Correspondence: cjj@szu.edu.cn (J.C.); shaoyh@szu.edu.cn (Y.S.)

Abstract: Surface plasmon resonance microscopy (SPRM) is a versatile technique for biosensing and imaging that facilitates high-sensitivity, label-free, real-time characterization. To date, SPR technology has been successfully commercialized and its performance has continued to improve. However, this method is inhibited by low spatial resolution and the inability to achieve single-molecule detection. In this report, we present an overview of SPRM research progress in the field of plasma imaging and sensing. A brief review of the technological advances in SPRM is outlined, as well as research progress in important applications. The combination of various new techniques with SPRM is emphasized. Finally, the current challenges and outlook of this technique are discussed.

Keywords: surface plasmon resonance microscopy; spatial resolution; surface plasmon resonance; biosensor



Citation: Huang, S.; Chen, J.; Zhang, T.; Dai, X.; Wang, X.; Zhou, J.; Kong, W.; Liu, Q.; Qu, J.; Shao, Y. Recent Advances in Surface Plasmon Resonance Microscopy. *Chemosensors* **2022**, *10*, 509. <https://doi.org/10.3390/chemosensors10120509>

Academic Editor: Ambra Giannetti

Received: 27 October 2022

Accepted: 28 November 2022

Published: 30 November 2022

Publisher's Note: MDPI stays neutral with regard to jurisdictional claims in published maps and institutional affiliations.



Copyright: © 2022 by the authors. Licensee MDPI, Basel, Switzerland. This article is an open access article distributed under the terms and conditions of the Creative Commons Attribution (CC BY) license (<https://creativecommons.org/licenses/by/4.0/>).

1. Introduction

Surface plasmon resonance (SPR) sensing technology facilitates real-time, label-free, high-sensitivity characterization and is a crucial tool for analyzing the binding dynamics among biomolecules. SPR has many applications in biomedical, mechanical, and chemical fields, such as investigating biomolecular interactions [1], gas detection, etc. The phenomenon of surface plasmon resonance was first discovered in 1902 by Wood, who observed it by illuminating polarized light onto a metal substrate diffraction grating [2]. In 1960, Stern and Farrell studied the conditions of the phenomenon and introduced the concept of “surface plasmon resonance” for the first time.

However, the lack of imaging capability of conventional SPR techniques has hindered their broad adoption. Fortunately, image acquisition using a digital camera is feasible for SPR technology, in which each image pixel can serve as an independent SPR sensing channel. Thus, imaging facilitates the exploitation of SPR-based techniques for high-throughput analysis.

Over the past decade, surface plasmon resonance imaging (SPRi) has enabled high-throughput, real-time, noninvasive biosensing in two-dimensional (2D) microarrays and simultaneous monitoring of several biomolecular interactions. It has been frequently applied to determine the specificity, affinity, and kinetic parameters of protein-protein, protein-DNA, receptor drug-virus, and other macromolecular binding processes [3–6].

The most commonly used prism-based SPRi instruments have sufficient spatial resolution to quantify independent sensing performance from numerous microfluidic channels [7], thus serving as useful tools for high-throughput multiplexed analysis in biological research and drug discovery [8–12]. Nevertheless, the spatial resolution of these systems is limited when the detected light is collected with regular, low numerical aperture (NA) lenses. Moreover, the signals obtained using these methods usually involve integration, since they are a collection of multiple interactions. Thus, the heterogeneity and microscopic details are obscured, thereby inhibiting single-cell or even single-molecule level measurements.

Therefore, it is vital to increase the spatial resolution of SPR techniques for molecular level detection. The spatial resolution can usually be significantly improved by incorporat-

ing an objective lens into the imaging system or by substituting the prism with a high-NA objective lens, which is called SPR microscopy (SPRM).

An early SPRM technique was developed based on the Kretschmann structure with the addition of a microscopic optical path for the reflected light imaging [13]. In recent years, the trend has been to combine integration-based spectral monitoring with high-NA optical microscopy to achieve single-molecule sensitivity [14]. Numerous applications have been made possible by this development. Although the spatial resolution of SPRM is sufficient to facilitate detection at the single-molecule level, point spread function (PSF) asymmetry is a problem, e.g., the SPRM snapshot of a circular nanostructure has a parabolic trail with several micrometers in the longitudinal direction. This phenomenon occurs because the plane waves generated by the plasma propagating along the surface of the gold film are coherently superimposed with the scattering field of the nanoparticles. In the case of wave vector matching, standing waves are generated at positions with opposite wave vector directions and the stripes become denser. The phase difference is constant at positions with the same wave vector direction and the stripes are in the same state, so the PSF exhibits parabolic trailing.

In addition, with the advancement of various new technologies, novel ideas and developments have been realized for SPR sensing, leading to improved performance and increased functionality. SPRM has been widely used to detect individual DNA molecules, characterize in situ binding kinetics of membrane proteins, track the dynamics of intracellular organelles, etc. This technique has developed a bridge between molecular level bio-interaction monitoring and high-resolution bio-imaging.

In this work, we review the principles and common operating systems of SPRM. In addition, recent advances in various kinds of novel SPRM technology are described. The applications of SPRM technology in biosensing are summarized. Finally, the challenges and outlook of the technology are discussed.

2. Principle and Configurations of SPRM

2.1. Principle of SPRM

The SPR phenomenon is generated by the collision of incident light with the free conduction electrons near the interface of two media (e.g., metal and dielectric medium) with opposite signs for the dielectric constant. A surface plasmon wave (SPW) is a transverse magnetic wave (TMW) produced by fluctuations in the charge density of free electrons at the metal surface, propagating parallel to the interface, with its energy decaying exponentially and vertically toward the surface. The electric field oscillation between SPWs and light waves occurs only in the TM mode, i.e., p-polarized. To resonate with the SPW, the incident light must satisfy certain conditions, and its wave vector component should be parallel to the metal-dielectric interface. The SPW propagation constant at the metal-dielectric surface can be written as [15]:

$$k_{\text{SP}} = \frac{\omega}{c} \sqrt{\frac{\epsilon_m \epsilon_g}{\epsilon_m + \epsilon_g}} \quad (1)$$

where ϵ_g is the metal's complex dielectric function, ϵ_m is the dielectric function of the adjacent medium, k_{SP} is the wave vector of the SPW, ω is the angular frequency of the wave, c is the speed of light in a vacuum, and ω/c is the wave vector in a vacuum. The wave vector of incident p-polarized light can be characterized as follows [16]:

$$k_{\text{in}} = \frac{\omega}{c} \sin \theta \quad (2)$$

where θ is the incident light's angle with respect to the metal-dielectric interface normal. Incident light on a smooth metallic surface cannot directly excite the SPW because the value of k_{in} is always smaller than the value of k_{SP} . The value of k_{in} can be increased via coupling with optical components such as prisms and gratings. Kretschmann proposed

the prism-coupling approach [17], which is based on attenuated total reflection (ATR). The wave vector is given as follows:

$$k_{\text{ATR}} = \frac{\omega}{c} \sin \theta \sqrt{\varepsilon_p} \quad (3)$$

where ε_p is the dielectric constant of the prism. When $k_{\text{SP}} = k_{\text{ATR}}$, the wave vectors of the incident light and SPW are matched. This is characterized by the coupling of the energy of incident photons to the SPW, contributing to the attenuation of the total internal reflection light and an absorption peak. The SPR dip angle or resonance angle (θ_R) appears at the position of the least reflected light intensity. Note that it is related to the refractive index (RI) of the medium; therefore, the medium can be reflected by changes in SPR characteristics.

A typical SPRM optical configuration consists of an excitation light source, an inverted microscope, and a CCD to acquire images. The operating process involves exciting the SPW by directing a p-polarized beam into a high-NA oil-immersion objective, focusing it onto the back focal plane of the objective, and illuminating a gold film to excite the SPR phenomenon. The incident illumination angle θ is changed by the lateral shift d of the beam staggering the system's optical axis and f is the focal length of the objective lens. The illumination angle is given by:

$$d = f \sin \theta \quad (4)$$

When the SPR phenomenon occurs, a sharp reduction of the reflected light intensity becomes recorded by the CCD through the objective. The resonance angle θ_R can be expressed as follows:

$$\sin \theta_R = \sqrt{\frac{\varepsilon_m \varepsilon_g}{(\varepsilon_m + \varepsilon_g) \varepsilon_o}} \quad (5)$$

where ε_o is the dielectric constant of the objective. Conventional SPR biosensor measurements are usually performed on samples with high coverage and weak scattering, which are analyzed using a layered dielectric model. However, this description does not apply to individual small objects (e.g., molecules, viruses, and nanoparticles). Typically, when strongly scattering objects are placed near a metal surface, parabolic diffraction patterns are produced. At the prism-metal interface, the incident light undergoes three types of interaction, including partial reflection (E_r), partial absorption to excite SPW (E_{SP}), and scattering of the SPW propagating parallel to the surface by the object resulting in a scattered field (E_s). The mixture of the reflected, scattered, and SPW fields determines the intensity of light measured at any given point in the SPR photograph (I_{SPR}). In the image that CCD records, the total intensity can be expressed as follows [18]:

$$I_{\text{SPR}} = |E_r + E_{\text{SP}} + E_s|^2 = |E_{\text{SP}} + E_r|^2 + |E_s|^2 + 2\text{Re}\{E_s(E_{\text{SP}}^* + E_r^*)\} \quad (6)$$

where the homogeneous SPR baseline in the exclusion of particles is provided as the first term. For particles that are far smaller than the wavelength of the incident light, the second term is an expression for basic scattering, which is insignificant. The third term, which denotes a more complicated interaction between the signal and SPW, can be written as an exponentially decaying columnar oscillation with a parabolic striped pattern in the image plane.

2.2. Research Progress of SPRM Technologies

SPRM platforms are mainly classified as prism-based and objective-based, where the prism-based SPRM platform is usually based on the prism-coupling model proposed by Kretschmann (Figure 1A). Here, p-polarized light is used to irradiate the gold film using prism coupling, which is then reflected after excitation of the SPW. The modulated reflected light is gathered using a CCD for imaging. On the other hand, according to the different illumination methods, objective-based SPRM is categorized into wide-field illumination and point-scanning categories. The wide-field illumination type SPRM (Figure 1B) collimates

the parallel incident light from a fiber output using an achromatic lens. It is then converted into p-polarized light using a cubic polarizer and concentrated on the back focal plane of objective lens. The focusing light is collimated by the objective to irradiate the sensing surface at an angle greater than total reflection and reflect it in a parallel light mode. The modulated reflected light is picked up by the symmetrical position of the objective and recorded by the CCD with an imaging lens. The use of high-NA objectives is limited in a prism-based SPRM owing to the optical path inside the prism. Compared to a prism-based SPRM, wide-field illuminated SPRM uses a high-NA objective to collect reflected light with higher spatial resolution, but does not reach the diffraction limit at the submicron level, whereas point-scanning SPRM has a higher value. In point-scanning SPRM (Figure 1C), the incident light is expanded and collimated by a pair of lens, and the pupil of the objective is illuminated. The beam is focused onto the interface between the sensor chip and the sample, and the reflected beam is collected. A polarizer is used to generate linearly polarized light, a neutral density filter regulates the beam intensity, and the sample is fitted on a three-dimensional piezoelectric stage with a feedback system that allows the beam to scan across the sample plane. Using a circular, axisymmetric, parallel incident light, Kano et al. found that the excited SPWs moved in multiple directions on the surface [19] and interfered with one another. At the geometric focus of the objective, a local electric field is formed. Scanning point by point in the sample plane can help to enhance spatial resolution. In this work, the authors used a CCD to record the reflected light at each point and then calculated the Fourier spectrum of the reflected light, which was then demodulated to obtain the RI of the sensing material on the surface of the gold film. The RI in the sensing material can reflect the thickness of the sensing material. Variations in film thickness change the effective permittivity of the near-field metal surface, which in turn changes the RI. In addition, the Fourier spectrum of the reflected light has two dark arcs. This is the characteristic pattern of SPW excitation. The radii of the curvatures of the arcs vary with the relative permittivity of the sensing material. To enhance the image contrast, Somekh et al., proposed a scanning epi-interference microscope by adding a z-direction motion to the two-dimensional scan. By moving the sample out of focus, the contrast was enhanced [20]. When the sample is not in objective's focal plane, two main output signals are generated, one from the SPW and the other from the light that is directly reflected after the sample is vertically irradiated. Meanwhile, the phase difference between the light propagating along pathways A and B will change (Figure 1D). However, these beams do not directly intersect, as they are positioned at different sites. Using an interferometer, the beams from routes A and B are combined with a common reference signal, and the amplitude of the total interferometric spectrum oscillates with the phase change between routes A and B, with a period that depends on the angle of incidence when the SPW is excited. Scanning epi-interferometers consist of a reference arm and a sample arm, with stringent requirements in terms of system stability. Therefore, Zhang et al. built a point-scan SPRM using a confocal optical path to provide a more compact and stable alternative that is compatible with commercial instruments. A spatial light modulator (SLM) can be used to control the optical pupil function and suppress light that interferes with the result, allowing a sample to be illuminated through a large range of angles [21].

Compared to wide-field illumination SPRMs, point-scanning SPRMs have higher spatial resolution but are slower. When conducting biological experiments, the ability to monitor a process in real time is an important capability, for which wide-field illumination SPRMs are more suitable.

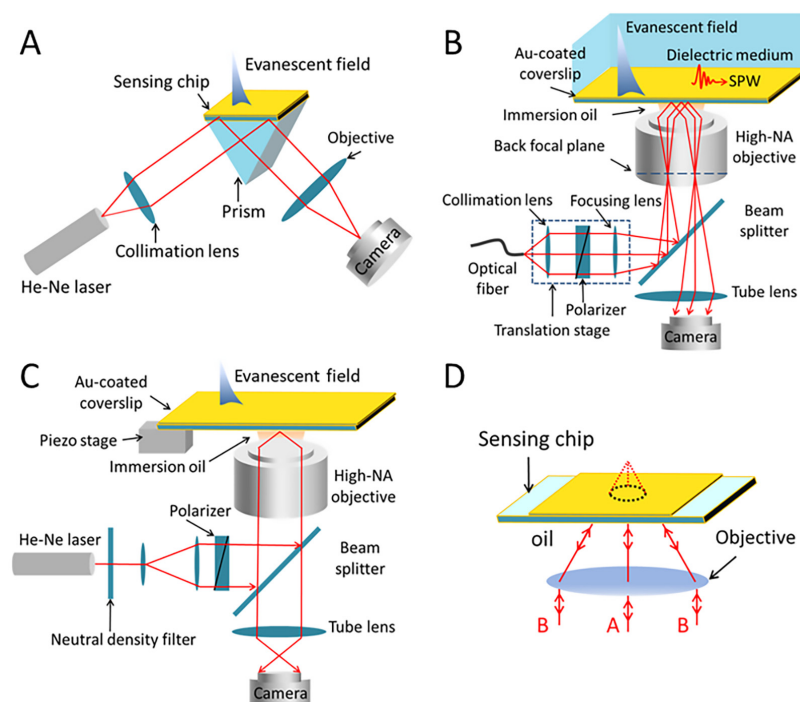


Figure 1. (A) Schematic of prism-based SPRM. (B) Schematic of wide-field illumination SPRM based on the objective lens. (C) Schematic of point-scanning SPRM based on an objective lens. (D) Schematic diagram showing the principal ray paths when the sample is defocused.

2.3. SPRM's Resolution Enhancement Methods

Although the application of high-NA objectives enables conventional SPRM to perform imaging and detection at the single-molecule level, its complex, parabolic-shaped PSF severely limits the spatial resolution and sensitivity. Owing to propagation of the SPW, the spatial resolution of the SPRM is different in the two directions (x - y direction), as it propagates on the chip's plane, which interferes with the images of nearby points and affects the resolution. The use of high-NA objectives guarantees that the x -direction resolution of the SPRM is diffraction-limited, but does not improve the resolution in the y -direction. Typically, the y -direction resolution is limited by the propagation length of the SPW, which is a number of microns.

From both the optical and computational perspectives, it is necessary to reconstruct a symmetric PSF, which relies on y -direction resolution and reducing the propagation length of the SPW. Notably, one way to enhance spatial resolution is to excite the SPW with a shorter wavelength of light [14]. In this work, the damping of the SPW in metal films was increased by using short-wavelength optical excitation to reduce the propagation length of the SPW. Thus, by comparing the excitation of SPW in gold films using 638 nm and 532 nm light sources, the SPW propagation length in water was found to be 3.1 μm and 0.2 μm , respectively. However, the spatial resolution can also be improved by obtaining SPRM images by scanning a focused laser beam point by point on the chip plane [22], in which case, the x -direction resolution can reach ~ 170 nm. However, mechanically scanning the laser beam inevitably reduces the temporal resolution, which is needed to investigate fast-binding kinetics and surface processes.

High spatial resolution SPR images can be achieved via azimuthal rotational illumination (ARI) [23], a method known as SPRM-ARI. With an effective time resolution that is only constrained by the illumination rotation speed (1 ms), this method offers an order of magnitude resolution improvement over conventional SPRM. In this work, the authors used ARI to allow for the excitation of SPWs on a silver surface along multiple azimuthal directions. This implied that the streaks or tails caused by the scattered SPWs could be azimuthally averaged (Figure 2A). The spatial resolution is enhanced because the nanospheres seem

to be much brighter than other areas. The parabolic PSF vanishes in a single nanosphere image, leaving only two tiny, closed bright spots (Figure 2B). Based on the PSF of surface plasmon coupled emission microscopy (SPCEM), the cause of these images can be identified [24]. In addition, the advantages of enhanced spatial resolution and interference fringe map smoothing by SPRM-ARI were further demonstrated by imaging a winding polymer nanowire with complex shapes using conventional SPRM and SPRM-ARI (Figure 2B). The former resulted in multiple fringes and scattering noise, which increased the difficulty of identification. Son et al. proposed a dual-channel spatially switched SPRM (ssSPRM) that significantly improved the image resolution in SPRM by a factor of nearly 15 compared to conventional SPRM [25]. In their work, dual-channel illumination switching was achieved in the reverse direction to the incident light while maintaining the incident and polarization angles (Figure 2C). Moreover, image reconstruction in dual-channel ssSPRM has been performed using the minimum filtering method. In this approach, the intensity of the corresponding pixels was compared separately in images with opposite incident directions. Small pixels were used to remove the most dominant scattering component, which greatly improved the spatial resolution of the image. Recently, Son et al., improved the two-channel method by proposing multichannel switching [26]. The multi-channel switching method refers to the spatial frequency sampling of an object field by continuously changing the direction of the incident illumination light. This method improves image sharpness and achieves robust and consistent imaging performance under various geometries. Notably, multi-channel optical switching in SPRM can significantly reduce the unfavorable scattering effect of SPWs and substantially improve image quality. Briefly, ignoring various limitations, an increase in the number of channels always leads to an increase in image quality. An analogy can be found in structured illumination microscopy (SIM), i.e., ssSPM with a larger number of channels represents a sampling of a larger area in Fourier space. Moreover, the image contrast is 3 times more enhanced than conventional SPRM.

The image reconstruction algorithm can reconstruct an isotropic PSF without sacrificing temporal resolution, but the complexity of the optical system is increased [27]. In the reconstruction process, the CCD records the reflected light from the chip surface, including the planar SPW E_p and the scattered SPW E_{SC} . In particular, the interference between SPWs is recorded in imaging mode. The scattered field is then obtained from the interference pattern by multiplying the SPRM image by E_p and applying a filter in the Fourier space using a method similar to optical holography. Notably, the PSF of the SPRM can be expressed as an attenuated columnar wave. The scattered field is deconvoluted with the PSF to obtain the target image. This method was demonstrated using 100 nm polystyrene nanoparticles, resulting in a 3-fold increase in the y-direction resolution, which reached ~310 nm in both the x and y directions. Nonetheless, the method calculates the scattered waves by assuming a single scattering of surface plasmon waves on the object's surface, which is unsuitable when multiple scattering is not negligible. In such a case, more sophisticated algorithms are required. The aforementioned image reconstruction algorithm is also used in another optimized SPRM instrument, wherein the reflected light interferes with a portion of the scattered light from the target object, which is then collected by a CMOS camera in a process called interferometric plasmonic microscopy (iPM) [28]. The method has a spatial resolution of ~260 nm and can image a single exosome adsorbed on the surface of the modified gold chip in real time. Moreover, the exosome's diameter (30–150 nm) can be determined according to the image intensity.

Compared to the poor longitudinal resolution of SPRM, the constraint of the metal-dielectric interface to the surface plasma results in very high axial sensitivity (z-direction). Owing to the rapid decay of SPW energy in the axial direction, SPW intensity is exponentially related to the perpendicular distance from the particle to the chip plane. This relationship can be converted by the decay constant of the SPRM system, which is capable of achieving an accuracy of ~5 nm in the axial direction [29]. In addition, an accuracy of ~0.1 nm can be obtained by the vertical oscillation of the nanoparticles [30].

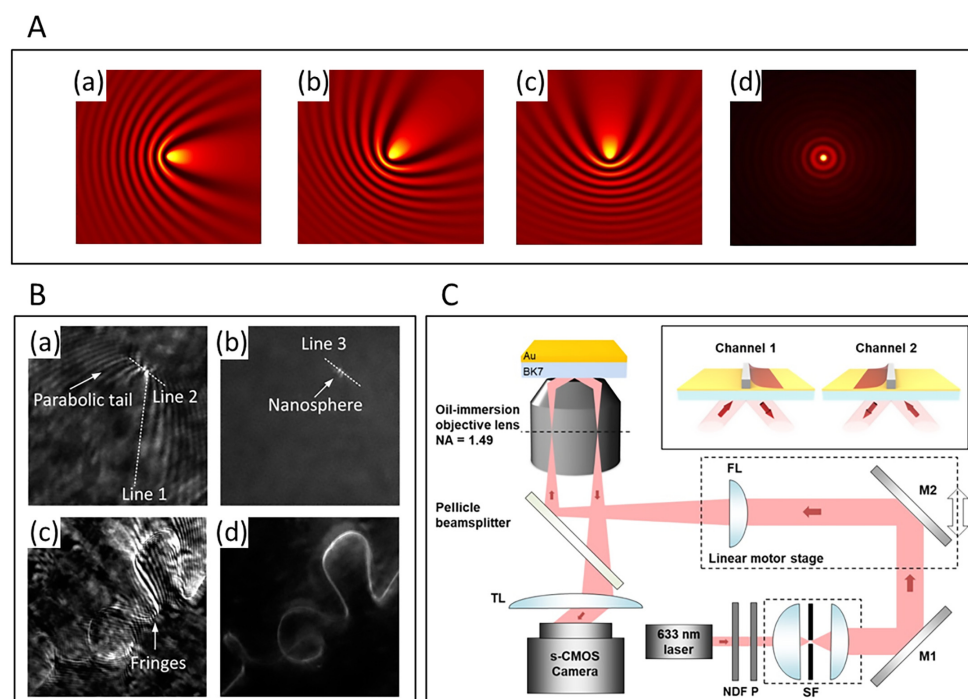


Figure 2. (A) Diagram demonstrating the overlap of incident plane waves at different azimuthal angles and circular scattered waves from a nanosphere [23]. In (d), comparable to the illumination source used in SPRM-ARI, the planar wave rotates in its propagation direction from 0° to 360° . (B) Images acquired using conventional SPRM (a,c) and SPRM-ARI (b,d) [23]. A nanosphere with a diameter of approximately 50 nm (a,b) and a winding polymer nanowire (c,d) were placed on the Ag film. Copyright 2019 Sci Adv. (C) Schematic of the optical setup of ssSPRM [25]. The inset is a conceptual illustration of switching in the ssSPRM. Copyright 2018 Opt Lett.

3. Advances in Biological Detection

Although the parabolic PSF limits the spatial resolution of SPRM, its unique advantages have resulted in its wide adoption in several fields.

3.1. Live Cell Studies

SPRM allows for the visualization of cellular activity and morphology. For example, the strength of cell-substrate adhesion has been assessed using this approach [31]. The study of cell-matrix interactions at the individual cell level is essential for understanding many aspects of cell behavior. Wang et al. achieved spatial mapping of local cell-matrix adhesion strength by monitoring cellular responses to controlled stimuli. In this work, they investigated the entire dynamic process of cellular response to extracellular osmotic pressure and obtained the spatial distribution of cell-substrate adhesion strength based on SPRM images (Figure 3A).

Our group presented the results of wavelength-scanning surface plasmon resonance microscopy (WS-SPRM) as an efficient analytical method for measuring cell-matrix interactions for the first time [32]. This approach facilitated real-time monitoring of changes in cell behavior during cell isolation under chemical and electroporation stimulation. Compared to intensity surface plasmon resonance microscopy (I-SPRM), WS-SPRM has a greater dynamic range (Figure 3B). The system consists of two optical paths (Figure 3B): the SPRM optical path under the sample stage and the white-light microscopy optical path above the sample stage. In the SPRM path, a liquid crystal tunable filter (LCTF) is used for fast and flexible wavelength scanning to achieve SPR imaging cycles within 1 s. When a scan cycle is completed, the SPR response value for each pixel point can be built from a series of images, i.e., the resonant wavelength (RW) of each pixel point can be obtained, enabling RW imaging of the gold plane. In the white-light microscopy path, incident light is scattered

and reflected by the cell, which is then collected by a CMOS camera during imaging. Using RW imaging of WS-SPRM to monitor cell detachment under trypsin stimulation, it was determined that the RW of the cell decreased when trypsin acted on the cell. A smaller cell adhesion area was observed owing to contraction of the cell, and for most of the area, the RW decreased to the background RW after 80 s of treatment. Finally, the cell eventually appeared as a small dot (Figure 3B). In addition, an imaging comparison between I-SPRM and WS-SPRM was also performed, and it was observed that the RI dynamic detection range of the cells calculated by WS-SPRM was approximately 3.5×10^{-2} RIU, whereas for I-SPRM, it was approximately 1.85×10^{-2} RIU. Obviously, a larger dynamic range accurately provides a more realistic image of the sensor surface. In summary, this label-free, non-invasive technique can measure the adhesion strength of cell substrates under natural conditions, thus minimizing damage to cell behavior from external forces.

Compared to wavelength interrogation SPR, phase interrogation SPR has higher detection sensitivity, and this technique has also been applied to SPRM. Zhang et al., developed a common-path digital holographic microscope (DHM) based on prism-coupled SPR phase imaging [33]. To achieve off-axis holographic recording, a beam splitter with a special structure was introduced into the SPR imaging system, which allowed the target and reference beams to propagate almost simultaneously in the system with excellent temporal stability (Figure 3C). Measuring the phase difference of reflected light in the case of SPR has significant advantages in achieving near-field RI and high-contrast phase imaging. A polynomial fitting equation was used to directly calculate the amount of RI change associated with the measured phase difference. When high temporal stability and phase curvature compensation were utilized, this system exhibited good performance in monitoring small RI changes and imaging biological tissues (Figure 3C). Dou et al., improved SPR holographic microscopy (SPRHM) by proposing a dual-channel illumination approach to increase the spatial resolution [34]. In the system, two incident beams traveling in opposite directions excite the SPR (Figure 3D). Using the polarization multiplexing technique of DHM, two off-axis holograms are created when the reference and target components of the two incident beams interfere with one another. After numerical reconstruction of the target wave, a weighted mean filtering algorithm was proposed for image synthesis to obtain SPR phase images with improved resolution up to $\sim 1 \mu\text{m}$ at 632.8 nm. This is comparable to the resolution of conventional optical microscopy with the advantages of wide field-of-view imaging and the high measurement sensitivity of SPR.

To study cellular micromotion, the detection distance can be extended using long-range SPR (LRSPR), which is typically 100–200 nm for conventional SPR and up to 500–1000 nm for LRSPR [35]. LRSPR was made possible by introducing a buffer layer with an RI similar to that of the sample, which was suspended between the substrate and the metal layer. In particular, the symmetric plasma structure induced coupling of the SPWs on both sides of the metal layer, thus allowing the SPWs to support an electromagnetic field markedly deeper into the sensing medium compared to conventional SPR. Furthermore, LRSPR can facilitate sensitive non-invasive measurements of the dynamic fluctuations of adherent cells, whereas conventional SPR is insensitive to such microwave motions.

SPRM can also map the binding kinetics of membrane proteins [36]. Membrane proteins direct multiple cellular responses to extracellular signals and have been intensively studied owing to their values as disease biomarkers and therapeutic targets. However, traditional methods used to isolate membrane proteins and perform non-in situ studies do not accurately reflect their intrinsic structure and function. Therefore, the high temporal and spatial resolution and label-free properties of SPRM render it an excellent imaging instrument for in situ studies of the binding kinetics of living cells. The images acquired via SPRM can be used to quantify the distribution of glycoproteins, which can then be fitted pixel by pixel using a first-level kinetic model that reflects local binding and dissociation rate constants.

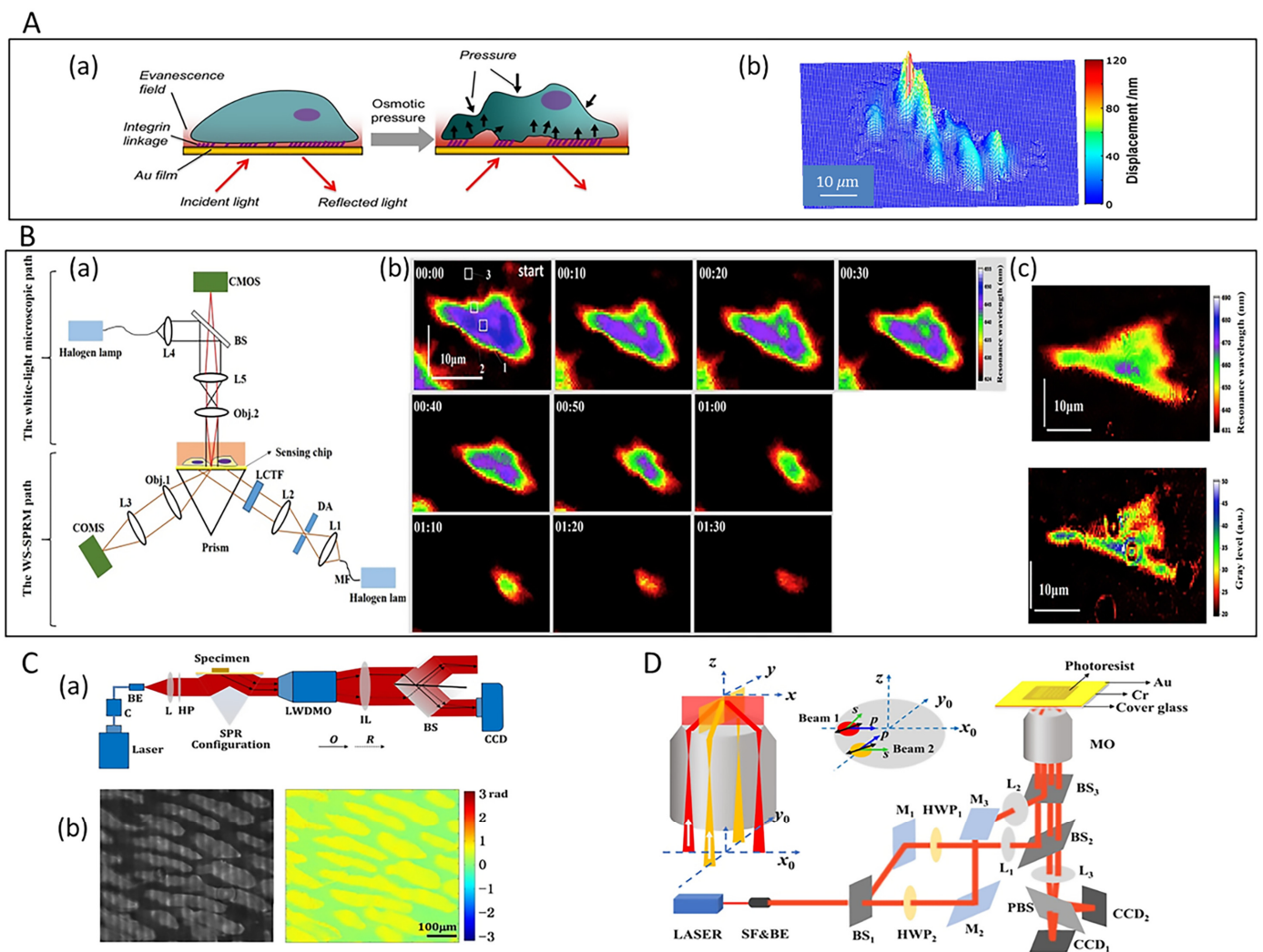


Figure 3. (A) Mapping cell-substrate interactions using SPRM [31]. (a) The osmotic pressure causes the bottom surface of the cells to face towards or away from the substrate. (b) Plotting the strength of cell-substrate adhesion, with larger displacements reflecting weaker adhesions. Copyright 2012 Langmuir. (B) Wavelength-scanning surface plasmon resonance microscopy [32]. The diagram of the WS-SPRM setup is shown in (a). (b) The RW images of a single cell undergoing trypsinization. (c) Dynamic range comparison of WS-SPRM and I-SPRM. Copyright 2019 Biosens Bioelectron. (C) The common-path DHM based on prism-coupling SPRM for onion tissue imaging [33]. Optical setup of the common-path DHM in (a), and experiment results for the phase imaging of onion tissue in (b). Copyright 2017 Appl Opt. (D) Experimental setup of dual-channel illumination SPRHM [34]. Copyright 2021 Opt Lett.

3.2. Single-Virus and Single-Bacteria Imaging

Non-imaging techniques, which provide information regarding the size of viral particles based on the statistical analysis of many particles, are not appropriate for studying the binding affinity of viruses. In contrast, high-resolution SPRM can spatially distinguish individual viruses, allowing for the detailed study of these organisms and detection of multiple different viruses. Wang et al. applied SPRM to the imaging and measurement of the size and mass of individual viruses [37] (Figure 4A,B). The SPR intensity of a particle is proportional to its volume. To obtain the size of a virus, a calibration curve, i.e., the SPR intensity-volume curve, can be plotted using nanoparticles as a calibration standard (Figure 4C). Based on its protein and lipid content, the RI of the H1N1 influenza virus is approximately 1.48. Therefore, a correction is made using silica nanoparticles with an

RI of 1.46. Thus, the volume of a virus can be obtained from the calibration curve and the mass can then be obtained using the known density information. Therefore, the measured diameter of the H1N1 influenza virus was determined to be 109 ± 13 nm and the mass was 0.80 ± 0.35 fg.

The micromotion of bacteria is closely related to their life activities. Bacterial motility has been investigated using atomic force microscopy (AFM). In this approach, several hundred bacterial cells are fixed on a cantilever, from which a beam is deflected. The deflection is dependent on the micromotion of the bacterial cells, which are immobilized on the cantilever. However, this method does not facilitate the determination of the micromotion of a single bacterium. In contrast, the axial resolution of SPRM facilitates the analysis of microbial motions with nanoscale precision. Recently, Syal et al., used plasmonic imaging and tracking (PIT) techniques to link bacterial micromotion to bacterial metabolism and antibiotic action [38]. In this work, *E. coli* O157:H7 cells were immobilized on a gold surface (Figure 4D) and they produced parabolic-shaped patterns via SPW scattering, in which the red spot indicated the object location position and the parabolic streak was caused by the scattered light (Figure 4E). The SPR images of bacteria at different locations were recorded with different image contrasts owing to the micromotion of the bacterial cells perpendicular to the chip (z-direction). When bacteria were exposed to high bactericidal concentrations of antibiotics, the micromotion was significantly reduced, indicating bacterial death.

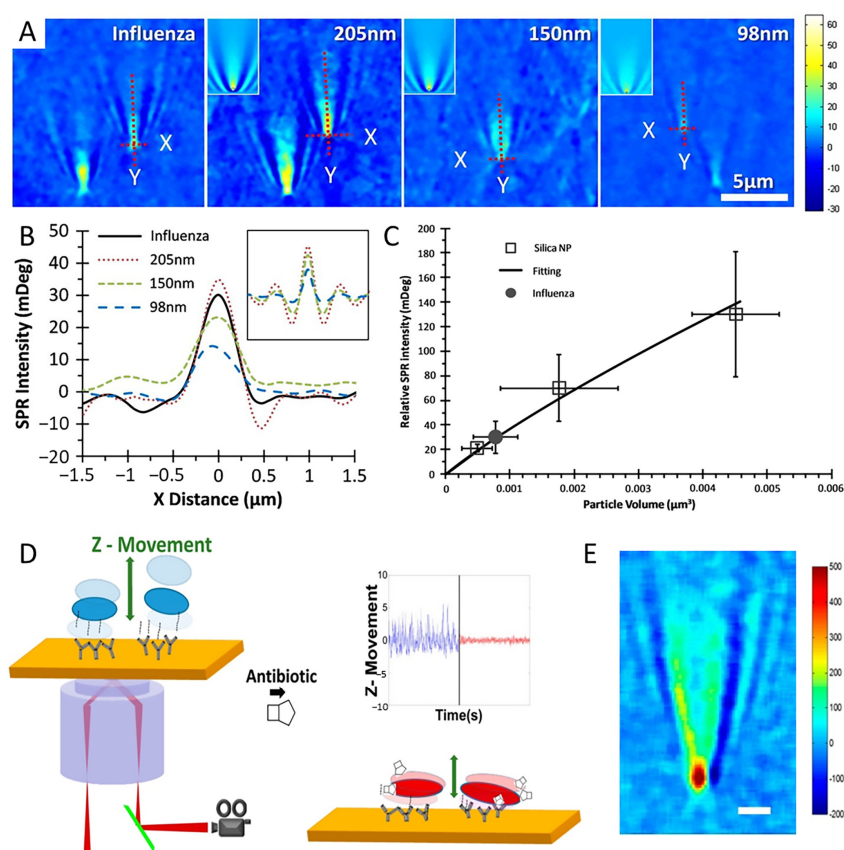


Figure 4. (A) SPRM images of H1N1 influenza A virus and silica nanoparticles [37]. (B) The SPR intensity profiles of selected particles along the x-direction [37]. The inset shows the corresponding profiles from simulated images. (C) Calibration curve of SPR intensity plotted vs. particle volume [37]. Copyright 2010 Proc Natl Acad Sci USA. (D) Setup and principle of SPRM imaging and tracking of bacterial cells tethered to a gold-coated glass sensor chip. Antibiotic action significantly suppressed bacterial motion [38]. (E) SPRM image of a bacterial cell [38]. Scale bar: 2 μm. Copyright 2016 ACS Nano.

3.3. Study of Biomolecules

The ability to image or visualize individual DNA molecules is fundamental to the advancement of a variety of applications of DNA. However, labeling DNA with fluorescent dyes can distort the original structure of DNA. Although AFM is a robust, label-free technique, scanning AFM probes may damage DNA samples. Yu et al., proposed a differential plasmonic imaging technique (DSPR) for label-free imaging of individual DNA molecules and measuring the length of individual DNA strands [39]. The method is based on the acquisition of two images obtained by translating the sample between two positions. Background noise removal is performed by subtracting one image from the other to obtain a differential image (Figure 5A). Subsequently, the scattering-based features are effectively removed using a deconvolution algorithm, and an image of the DNA sample without scattering effects is obtained (Figure 5B,C). Using this approach, the average length of a single stretched DNA molecule was determined to be approximately 14.6 μm . Therefore, SPRM is a label-free, quantitative approach that is suitable for single-DNA-molecule analysis.

This technique can be used to sensitively detect changes in RI near an interface, which is closely related to its molecular mass and volume. Based on small changes in the sensing surface mass, SPRM is one of the most effective tools for detecting interactions between biomolecules. The aforementioned studies involved intensity, wavelength, and phase interrogation SPRMs, among which the intensity type is the most widely used because of its straightforward optics. Tan et al., described a high-resolution quantitative angular scanning wide-field SPRM that was applied to the imaging of protein-antibody interactions in water media [40]. In this work, a laser disrupted the spatial coherence of a beam using a rotating diffuser, and higher quality images of smaller artifacts were acquired compared to the case of spatially coherent illumination. The illumination angle of the spatially incoherent light depends on the amplitude of the spatial light modulator (SLM) at the conjugate position of the back focal plane of the objective, enabling dynamic control of the illumination angle. Therefore, a series of wide-field SPR images are obtained.

SPRM is widely used in the field of biomolecular interactions, but its application for detecting small molecules remains challenging. Small molecules have a low mass, and when they bind to the detection surface, the change in RI is minimal. Therefore, the main strategy for detecting these molecules is to enhance the signal associated with biomolecular binding. In particular, the feasibility of enhancing the signal by labeling biomolecules with gold nanoparticles has been demonstrated. The introduction of gold nanoparticles leads to an increase in the mass of the sample, which results in a significant increase in the signal. Halpern et al. used this approach in combination with SPRM to detect the hybridization kinetics of DNA in real time [41]. In their investigation, the authors described a near-infrared, high-NA objective-coupled SPRM with two improvements. One improvement is that the use of the 814 nm wavelength reduces the SPR angle and improves SPR sensitivity compared to visible wavelengths. Although the longer propagation length of the NIR wave reduces the spatial resolution in the SPW propagation direction, a single nanoparticle can be localized by the unique resulting parabolic PSF. The second improvement is that a gold-coated knife-edge mirror is used to split the light. Notably, due to the application of the knife-edge mirror, the incident light can be split without loss of signal, which eliminates the potential interference effects associated with multiple reflections. DNA-modified gold nanoparticles at concentrations of 5–0.1 pM were detected on intact monolayers of complementary sequences by counting the binding events of individual nanoparticles (Figure 5D). Another method for detecting small molecules is plasmonic-based electrochemical impedance microscopy (P-EIM). P-EIM involves imaging the electrochemical impedance distribution over the entire plane using SPRM [42]. In particular, three images can be simultaneously obtained by applying potential modulation to the sensor's surface: the amplitude and phase of the AC component and the DC component. The DC component is the same as the conventional SPR image, which provides molecular binding information, while the AC component is related to the local impedance of the surface. The local amplitude and phase of the AC component are extracted using the FFT,

and amplitude and phase images are then obtained at different frequencies. P-EIM is used to detect small molecular charges [43]. In this work, the phase signal of the P-EIM is a function of the local surface charge. Notably, the difference between the phase components of small molecules and the dextran hydrogel sensor surface can be used to distinguish between small molecules, thus bypassing the mass limit (~ 100 Da) of conventional SPR measurements (Figure 5E).

Measuring the binding kinetics of individual proteins is also a challenging task. Zhang et al., modified a conventional SPRM to image the scattered SPWs in transmission mode, a method known as plasmonic scattering microscopy (PSM) [44]. The imaging principle of PSM is based on SPRM, whereby the SPWs are scattered by inhomogeneous gold film surfaces and proteins and subsequently interfere with one another. The interfering light is directly acquired for imaging, employing an additional objective positioned above the sample (Figure 6A). This avoids interference from strongly reflected light, which facilitates higher illumination intensities ($\sim 30,000\times$) and significantly improves image contrast. PSM images do not have parabolic PSFs, but rather complex bright spots. The image intensity is determined by integrating the intensity of all pixels, which is independent of the inhomogeneous background caused by the random distribution of the surface roughness (Figure 6B). In this study, the rapid binding and unbinding of molecules were observed, and the binding kinetics of a single molecule was then determined by obtaining the distribution of the bound and unbound state dwell times from the time-intensity maps of the bound and unbound states (Figure 6C,D). Recently, a PSM optical device was modified by Zhang et al. [45]. In this work, single-molecule imaging was implemented in the extensively employed, Kretschmann prism-coupling SPRM apparatus, while preserving single protein sensitivity and great spatial resolution. This method demonstrates a simpler application of high spatial resolution imaging in systems.

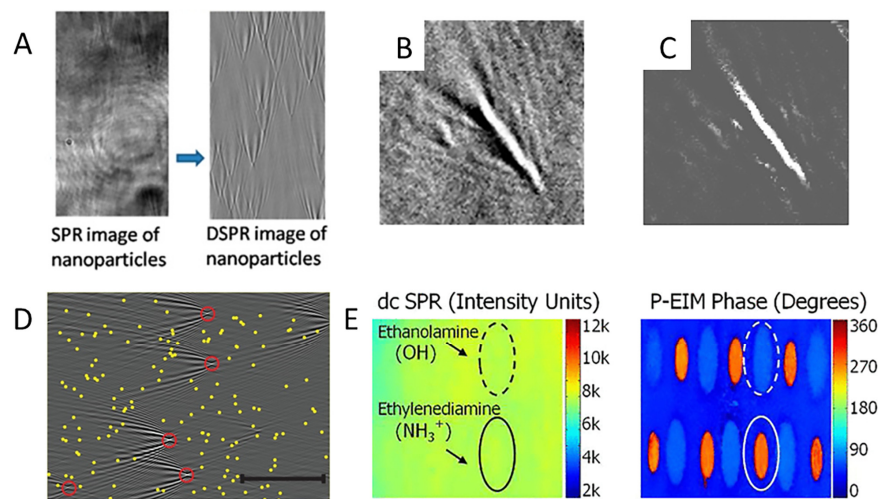


Figure 5. (A) Images of 80 nm platinum nanoparticles on bare gold film obtained using SPR and DSPR to illustrate the superior contrast enhancement of DSPR [39]. DSPR image of DNA molecules, before (B) and after (C) deconvolution [39]. Copyright 2014 ACS Nano. (D) Gold nanoparticles for signal amplification [41]. DSPR image of DNA-functionalized gold nanoparticles binding to a complementary surface. The image shows 5 binding events (red circles). The positions of all bound particles after 300 s are marked with yellow dots and are overlaid on the image. The scale bar is 25 μm . Copyright 2014 ACS Nano. (E) P-EIM signals of printed small molecules spots [43]. The DC component of the response is the average intensity, and the AC component consists of a phase and amplitude. Copyright 2013 Anal Chem.

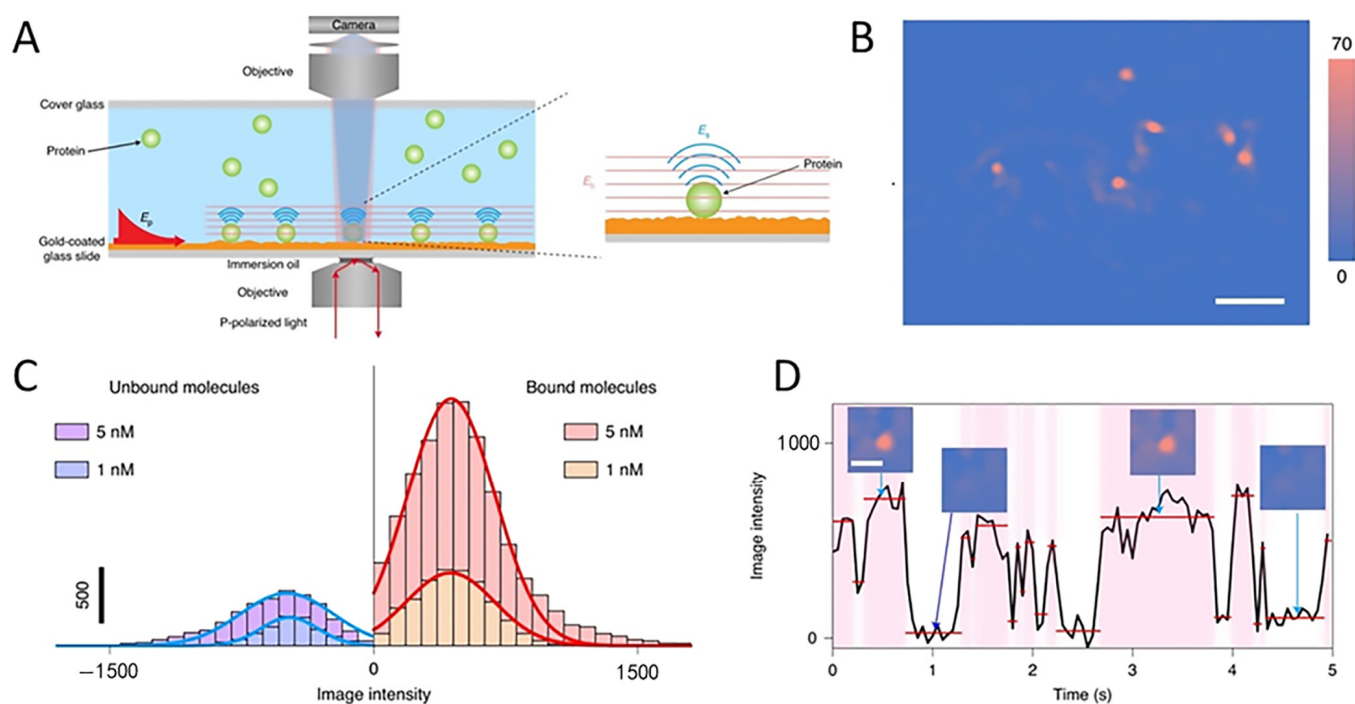


Figure 6. (A) The optical setup of PSM. The SPW (E_p) is excited by light from the bottom [44]. The scattered SPWs by a particle (E_s) and the gold surface (E_b) are collected above the sample to form a PSM image. (B) Background- and drift-corrected PSM image [44]. (C) Histograms exhibiting changes in intensity due to the binding and unbinding of individual IgA molecules [44]. (D) The binding behavior of a single IgA molecule [44]. Copyright 2020 Nat Methods.

4. Novel Technologies for SPRM Enhancement

4.1. Development of Multifunctional Nano-Oscillators

In addition to gold nanoparticle signal amplification and P-EIM methods, Shan et al. proposed a new approach for detecting small molecules, namely nano-oscillators, by combining the signal amplification associated with gold nanoparticles and P-EIM to achieve superior axial resolution [30]. In this work, each nano-oscillator is made up of a gold nanoparticle tethered to a gold coating by a chain of molecules, such as polyethylene glycol (PEG), with an appropriate linking group termination. The next step is to apply an AC voltage between the gold coating and a reference electrode embedded in the solution, establishing an alternating electric field orthogonal to the gold layer and capable of driving charged particles (Figure 7A). The selection of soft molecular chains allows it to stretch from a relaxed to a stretched state using a relatively tiny driving force, ensuring a large oscillation amplitude and thus an accurate charge sensitivity. Notably, the oscillator's oscillation amplitude can be recognized with an accuracy of ~ 0.1 nm using SPR imaging. Recently, Chen et al., improved this current-driven nano-oscillator [46]. In their study, the gold nanoparticles were tethered to the sensing surface by a polymer, which had a rigid stretching structure to support the nanoparticles at low temperatures. When the temperature increased to a threshold value, the polymer lost its rigid structure and the gold nanoparticles fell to the surface. The oscillation of the nano-oscillator was induced using periodic light illumination.

Nano-oscillators use gold nanoparticles to enhance signal strength; however, the enhancement effect can be achieved using other particles. Recently, Ma et al., used the nano-oscillator principle to replace gold nanoparticles with individual proteins, with indium tin oxide (ITO) as the surface, thereby quantifying the size, charge, and mobility of the protein [47]. In this work, proteins were immobilized on ITO slides using PEG and driven to oscillate vertically by applying an alternating electric field to the ITO surface. Using

an objective-based SPRM device, a CMOS detector collected the signal to form an image. The image series were then subjected to FFT to detach the oscillation frequency of the applied field and extract the oscillation amplitude, meanwhile rejecting the background noise. A linear relationship at low electric field strengths is shown in the plot of the FFT image contrast versus electric potential amplitude (Figure 7B). Therefore, the FFT contrast can be used to quantify the oscillation amplitude. The tethered proteins' size (Figure 7C), charge, mobility, and conformation were all assessed utilizing signals that were acquired. Subsequently, a plot of mobility versus size for several single proteins and protein-ligand complexes was created using these data (Figure 7D).

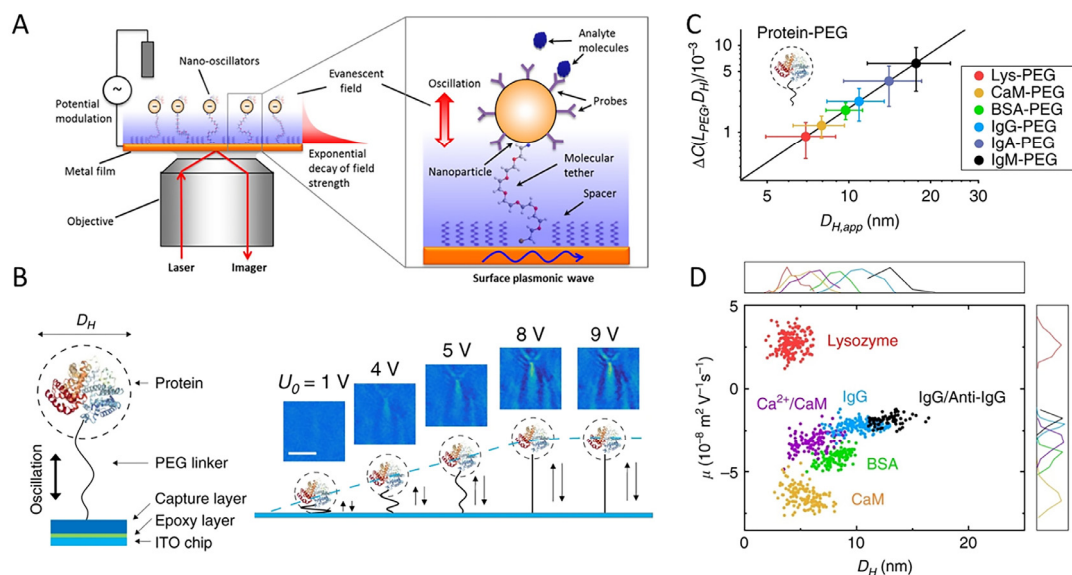


Figure 7. (A) Schematic of nano-oscillators on an Au electrode [30]. Copyright 2014 Nano Lett. (B) Schematic showing a single protein tethered to an ITO surface via a 63 nm long PEG linker, and the plot of the FFT image contrast vs. potential amplitude [47]. A linear relationship is observed at low electric fields and a plateau associated with full stretching of the PEG tether is exhibited at high electric fields. (C) Size calibration and determination of protein-PEG size (D_H), from the FFT image contrast change ΔC [47]. (D) 2D plot of mobility (μ) vs. size (D_H) of single proteins and protein–ligand complexes [47]. Copyright 2020 Nat Commun.

4.2. Applications of Machine Learning Algorithms in SPRM

Machine learning has been aggressively investigated in the field of biotechnology. Recently, Moon et al., used a deep learning approach to improve the performance of SPRM for light scattering detection [48]. In this work, a deep learning algorithm based on convolutional neural networks (CNN) was used to estimate the effect of scattering parameters, mainly, the number of scatterers. The CNN architecture consists of the convolution layer (Conv), batch normalization (BN), rectified linear unit (Relu), max pooling layer (Pooling), fully connected layer (FC), and output layer (Figure 8A). The method was applied to SPRM images formed by the coherent interference of scatterers, and the improvement was quantitatively evaluated. With the trained CNN, approximately 2000 SPW scattered images can be classified in less than 1 s, which means that the classification can be performed in real time after training. The method was applied to SPRM images formed by the coherent interference of scatterers, and the improvement was quantitatively evaluated. In particular, it was determined that the detection accuracy of deep learning was improved by a factor of almost six compared to traditional image reconstruction algorithms [27]. Identifying complex objects is difficult using traditional algorithms. The combined deep learning algorithm can effectively detect scattered targets in noisy environments. Furthermore, deep

learning can be directly extended to label-free molecular detection analysis, resulting in significantly improved detection in imaging and microscopy techniques.

Although SPRM provides excellent sensitivity, the statistical analysis of numerous nanoparticles is laborious and time-consuming. Moreover, reliable identification and quantification cannot be achieved when the image contrast is too low. Wang et al., proposed an image processing software package for nanoparticle analysis based on deep learning algorithms [49]. In their work, fully automated nanoparticle identification, digital counting, 3D tracking of particle position, and quantification of kinetic information were achieved at the single particle level (Figure 8B). Using a built-in image filtering algorithm [27] to remove mechanical and scattered particle noise, the image contrast was significantly improved, enabling robust identification and analysis of low-RI nanoparticles in SPRM images.

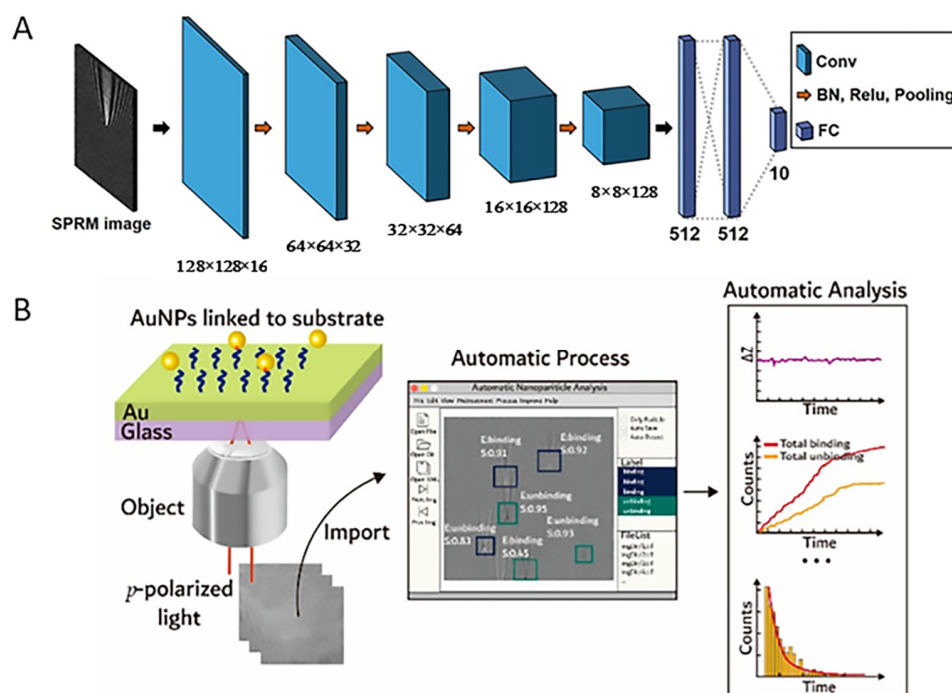


Figure 8. (A) Schematic diagram of the CNN architecture [48]. The network consists of the convolution layer (Conv), batch normalization (BN), rectified linear unit (Relu), max pooling layer (Pooling), fully connected layer (FC), and output layer. Copyright 2019 Anal Chem. (B) Schematic diagram of image processing software package for nanoparticle analysis in SPRM [49]. Automated nanoparticle identification, digital counting, 3D tracking of particle position, and quantification of kinetic information were achieved in this work. Copyright 2021 Anal Chem.

4.3. Integration of Optical Manipulation Technology

SPRM can non-invasively detect cell-substrate interactions at interfaces with high sensitivity. In the last decade, various sensitivity-enhancing biosensing methods have emerged, which can mainly be divided into two schemes: (1) the use of precision fabricated nanostructures to enhance sensitivity, and (2) the use of various active external forces to drive and enrich analytes.

Passively driven interactions are completely dependent on Brownian diffusion processes throughout the sensing time, which greatly hinders their efficiency. Our group proposed the optothermophoretic flipping (OTF) method, which significantly improved the sensitivity of SPRM sensing [50]. Photothermolysis manipulation techniques rely on photothermal conversion to form a temperature gradient field and manipulation is achieved via thermophoretic forces that cause objects to migrate directionally in the temperature gradient field [51]. The OTF method achieves protein-protein interaction enhancement by temporal modulation of the thermophoretic force and convective flow (two major forces),

which enriches biomolecules and results in aggregation to facilitate effective contact. In this work, the enrichment performance was tested using antibody-antigen binding with a wavelength-interrogation SPRM (W-SPRM) platform, which showed a 23.6-fold increase in sensitivity in biomolecular interaction sensing compared to interactions based on Brownian diffusion only. In addition, the experimental setup consisted of a W-SPRM component and an optothermal excitation component (Figure 9A). The process of enrichment regarding analytes involved the generation of a temperature distribution and thermal convection after turning on the heating laser. Convective flow and thermophoretic forces work together to migrate and enrich biomolecules to the ring region at relatively low temperatures when the laser is turned on, and the upward thermophoretic force leads to inefficient binding of biomolecules. When the laser is turned off, the flipped thermophoretic force (downward) induces efficient binding of biomolecules (Figure 9A). Notably, thermophoretic force flipping is due to the thermal conductivity difference between the Au film and the surrounding solution, i.e., the high thermal conductivity of gold leads to a faster heat dissipation rate in the gold film than in the solution. Therefore, in the transient time (tens of microseconds) after the heating laser is turned off, the temperature of the solution is higher than that of the gold film, and the temperature gradient in the z-direction is reversed. Thus, biomolecules can be pushed toward the sensing surface to achieve efficient binding. In addition to the enhanced intermolecular interaction probability, the real-time imaging capability of the W-SPRM device facilitates locating the most sensitive regions of biomolecular interactions and the selection and manipulation of the regions of interest for sensing. Furthermore, the application of the thermophoretic force of the photothermal effect can be applied to the optical tweezing technique for nanoparticle capture [52].

Optical tweezers typically focus a beam using a high-NA objective to generate a gradient force, thereby creating an optical potential well that is capable of capturing micro/nanometer-sized objects. SPRHM combines the SPR technique with DHM to obtain near-field SPR images with both amplitude and phase contrast. Recently, Dai et al. proposed an integrated optical tweezer technique for SPRHM (OT-SPRHM) that facilitates the dynamic description of cell-substrate interactions under optical excitation [53]. In this work, the authors constructed a compact OT-SPRHM system in which OT and SPRHM were arranged coaxially to enable simultaneous manipulation and detection of the same biological specimen, respectively (Figure 9B). Live K562 cells and MC3T3-E1 cells were manipulated via OT, and phase-contrast SPR images were recorded using SPRHM. In particular, this new platform determined the optical force applied to K562 cells near the cell-substrate interface (Figure 9B).

The combination of nanoparticles and nanostructures as sensing probes presents many new opportunities for traditional SPR sensing techniques. OT enables capturing objects of micro/nanometer size, while its focus point is a few hundred nanometers, which limits the accuracy of capture. Given that SPWs on metal surfaces exhibit large field enhancement compared to incident radiation and much smaller wavelengths than free space wavelengths, hot spots much smaller than free space wavelengths can be excited using SPR techniques. Under such constraints, the plasmon field helps to capture various nanostructures and materials with high precision. In recent years, plasmonic nano-tweezers (PNT) with the ability to manipulate nanoscale particles or molecules beyond the diffraction limit have been rapidly developed, and the combination of this technique with imaging techniques allows for the practical observation of local molecular interactions in biological samples and the monitoring of dynamic processes in biological samples with high spatial resolution, sensitivity, and throughput. However, some biomolecules are sensitive to temperature and high temperature may affect their activity, etc.; therefore, plasmonic heating limits the application of SPWs in capturing particles or biomolecules that are susceptible to high temperatures. For this reason, our group designed a nanorefrigerative tweezer based on a single refrigerative nanocrystal [54]. This scheme has the advantage of subwavelength-scale trapping, comparable to that of the PNT, while avoiding the undesirable effects of plasmonic heating.

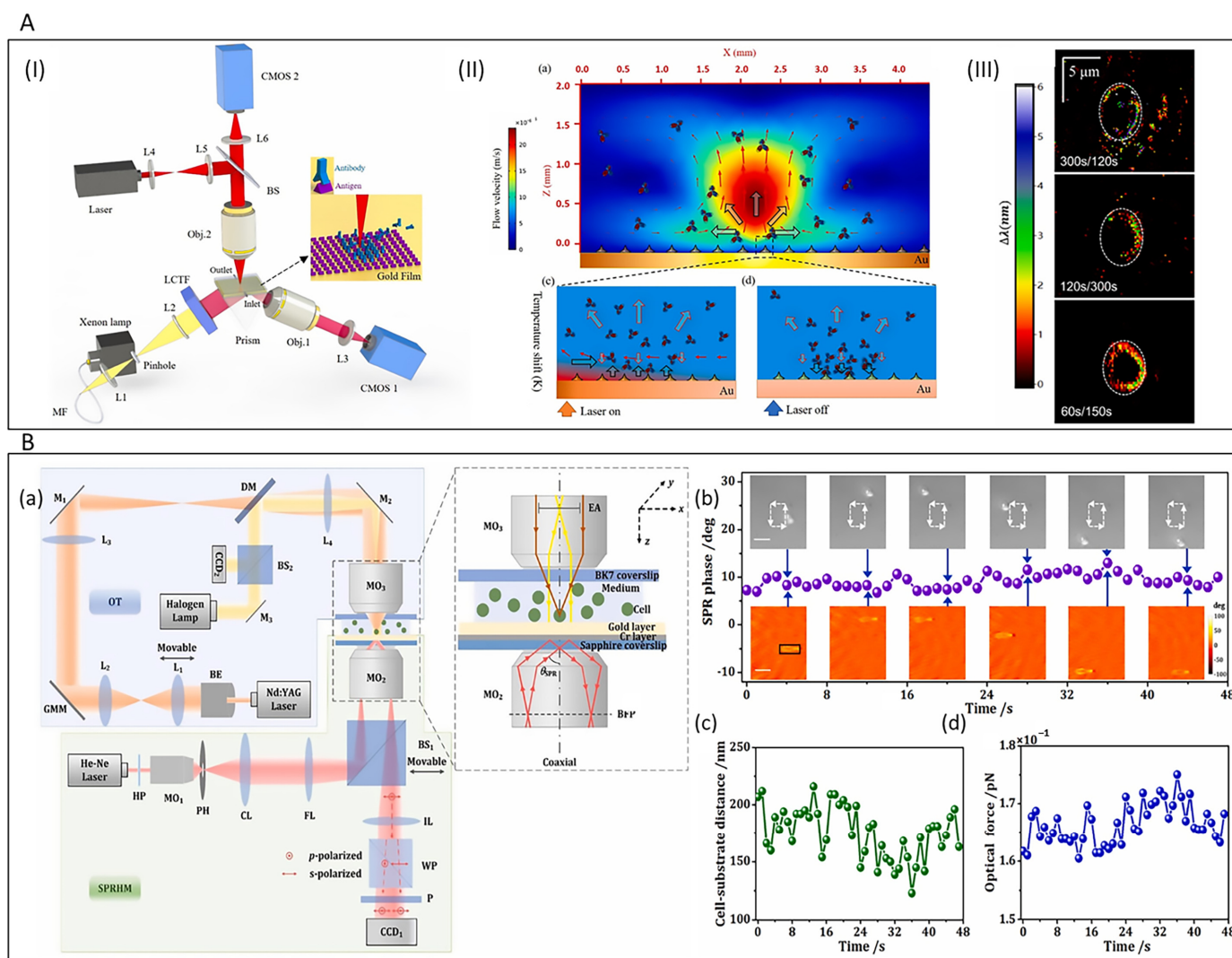


Figure 9. (A) Schematic diagram of the optical path of SPRM based on OTF and its principle [50]. (I) System optical path schematic. The W-SPRM part and optothermal excitation part. (II) Schematic diagram of OTF method for enrichment of biomolecules. (III) The OTF method effectively enriches biomolecules and achieves enhanced sensitivity. Copyright 2022 Biosens Bioelectron. (B) Schematic diagram of the optical path of OT-SPRHM (a) and cell manipulation phenomenon (b–d) [53]. Experimental results include (b) SPR phase of the cell, (c) cell-substrate distance, and (d) optical force applied to the cell versus time. Copyright 2022 Biosens Bioelectron.

4.4. Applications of Optical Vortex

Optical vortex beams can excite SPWs, thus allowing for the development of a new type of SPRM with the advantages of high resolution and sensitivity, which is a new approach for label-free, in situ, multi-modal detection of substances including biomolecules. Optical vortex beams can be divided into two categories depending on the different generation mechanisms: one is directly generated by a phase wavefront distribution with a spiral structure to produce a central phase singularity, and the other is generated by a polarization direction distribution with azimuthal variation to form a hollow beam, which are referred to as the orbital angular momentum beam and the vector beam, respectively.

Tan et al., demonstrated that an optical vortex beam focused on a metal surface with a vertical incidence can excite SPWs [55]. When the plane wave of the optical vortex beam is emitted from the objective and converges toward the geometric focus, a diffraction-limited spot is generated, which contains a large wave spectrum limited by the NA of the

objective and two opposite sets of plane waves with an incidence angle of $\pm\theta_{SP}$. At the sensing chip plane, it produces two $\pm k_{SP}$ reversed center-propagating SPWs with coherent superposition in the central region to form plasmonic standing waves. In addition, the SPR angle can be tuned by the radius of the vortex beam at different metal/dielectric interface structures. Moh et al. used this method to image cell substrates on SPRM structures [56]. This investigation was based on radially polarized light excitation of a localized surface plasmon resonance (LSPR) to form a virtual probe. The intensity distribution on the metal surface allowed for quantitative measurements of the cell-matrix contact, and the obtained data were presented as a local RI map (Figure 10A).

Radially polarized light is a vector beam with a strong focus and strong longitudinal component, which can form small and strong optical probes. The beam can be focused onto precious metal nanoparticles to produce LSPR, which generates an electromagnetic field that is localized around the particle's surface. In particular, when there is a gap between the particle and gold film surface, the LSPR and SPR on the surface are coupled and a regional electric field enhancement, i.e., Raman enhancement, occurs. This principle can be used to measure the vertical field by manipulating the particles via OT and using the Raman signal to characterize the vertical electric field components. Shen et al. presented the details of a dynamic single particle-gold film surface-enhanced Raman scattering (SERS) system, which was achieved by manipulating individual gold nanoparticles using PNT [57]. The experimental setup consisted of a PNT platform and signal acquisition system that created a circular plasmonic standing wave by focusing radially polarized light onto a thin sensing film. A virtual probe was used at the center of the interference, which acted as a PNT to capture the particles. In this work, it was demonstrated that the gap mode produced an additional enhancement of 10^{-4} compared to the film without the particles, eventually reaching a SERS enhancement of 10^{-9} . Based on nanomanipulation of the PNT, this dynamic single-particle thin-film system can facilitate controlled SERS detection in an aqueous environment. Recently, Dou et al. revealed the physical mechanism of the polarization-controlled plasmonic gap mode enhancement by comparing the SERS intensity of individual nanoparticle-film gap structures for different polarization beam excitations [58]. The results showed that the SERS signal can be significantly enhanced under radial polarization and substantially suppressed under azimuthal polarization compared to conventional linear polarization (Figure 10B). This was attributed to the different vertical electric field distributions of the SPWs. This work has important implications for single-particle SERS studies and quantitative molecular detection.

The SPR image can be altered by modulating the optical vortex beam to allow new applications. Hu et al., theoretically and experimentally investigated a method to generate and control dynamic SPR intensity images using a highly focused geared beam [59]. A geared beam is a donut beam with an entangled double-helix phase that is formed by the co-linear superposition of two Laguerre–Gaussian beams with equal but opposite topological charges (Figure 10C). Owing to the flexible nature of the optical vortex beam, this method can be used to easily pattern SPWs at predetermined locations and dynamically control the pattern. Thus, it is a good candidate for generating and controlling SPR local fields. Furthermore, Man et al. used a vector beam with an arbitrary local linear polarization state for dynamic plasmonic beam shaping [60]. In microscopy devices with high-NA objectives, the excitation, orientation, and distribution of the focused SPWs are highly dependent on the spatially variant polarization of the incident vector beam. Notably, when an axially symmetric vector beam is involved, multifocal SPWs with the same magnitude and uniform intensity can be obtained. Meanwhile, the number of focal points depends on the polarization order n (Figure 10D).

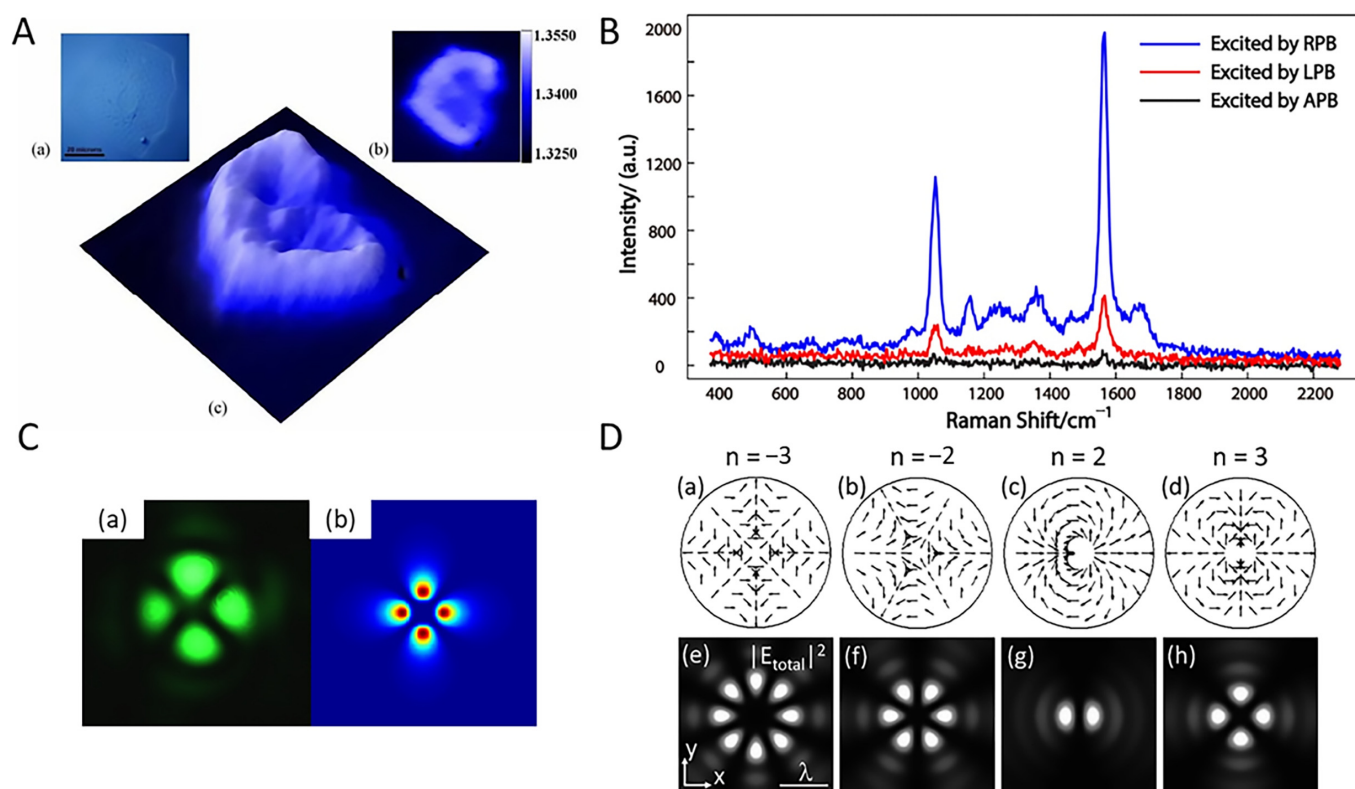


Figure 10. (A) SPRM with radially polarized beams [56]. A cheek cell observed under epi-illumination conditions in (a–c) is the obtained RI map of the same cell. Copyright 2008 Opt Express. (B) ERS signals measured for an incident linearly polarized beam (LPB), radially polarized beam (RPB), and azimuthally polarized beam (APB) for a single nanoparticle [58]. Copyright 2017 Journal of Physics D: Applied Physics. (C) Experimental (a) and simulation (b) results for a cogwheel beam [59]. Copyright 2008 Applied Physics Letters. (D) The higher order polarization modes [60]. (a–d) Distribution of the incident polarization mode with $n = -3, -2, 2,$ and 3 , and (e–h) the corresponding total intensity distribution of the SPWs. Copyright 2014 Applied Physics Letters.

5. Conclusions and Future Perspectives

In this review, we summarized the progress of SPRM research in systems and technologies and presented a range of applications involving biosensing and imaging, including living cells, bacteria, viruses, DNA molecules, and proteins. Recently, research on SPRM optical platforms has focused on achieving optimal spatial resolution. Although the technology has been shown to be feasible for detecting a variety of biological substances and processes, many challenges remain in improving its sensitivity, detection limits, and expanding its applications.

The lateral resolution of SPRM is diffraction-limited. In particular, the parabolic-shaped PSFs can be up to several microns in length and adversely affect image quality. To improve lateral resolution, numerous approaches have been proposed to optimize the optical system, such as SPW excitation using a short-wavelength laser, azimuthal rotational illumination, and image reconstruction algorithms. We expect that innovations in instrumentation and image processing algorithms will exploit the asymmetric PSF to extract more bio-interaction information, thereby allowing for further improvements in spatial resolution without sacrificing sensitivity or temporal resolution.

In addition, there have been significant advances in the technology and application of SPRM, but the technique is not yet commercially viable, in contrast with traditional SPR biosensors. Currently, only a few commercial SPRM platforms are available, which has resulted in a lack of standardization of instrumentation and measurement methods. Although SPRM platforms can meet the requirements for analyzing numerous biological

samples, the analysis of complex samples with ultra-low concentrations (<10 fM) is still challenging. Therefore, the combination of SPRM with external means of active manipulation, including active enhancement methods such as electrokinetic, electrochemical, optical, optothermal, magnetic, and acoustic manipulation, or from the materials side, including signal amplification tags and modifications of traditional substrates, may lead to the development of more sensitive and accurate SPRM platforms [61].

These challenges will eventually be addressed with future technical and theoretical developments, and it is expected that SPRM techniques will be more widely used and provide deeper insights into complex biological matter and behavior.

Author Contributions: Conceptualization, S.H. and J.C.; methodology, Y.S.; software, X.W.; validation, S.H., T.Z., X.D., J.Z., W.K. and Q.L.; formal analysis, S.H. and X.W.; investigation, S.H.; resources, J.C.; data curation, S.H.; writing—original draft preparation, S.H.; writing—review and edition, J.C. and Y.S.; visualization, J.C. and Y.S.; supervision, J.C., Y.S. and J.Q.; project administration, J.C. and Y.S.; funding acquisition, J.C. and Y.S. All authors have read and agreed to the published version of the manuscript.

Funding: This work was supported by the National Natural Science Foundation of China (62275168, 61905145, 62275164); Guangdong Natural Science Foundation and Province Project (2021A1515011916); and Shenzhen Science and Technology R&D and Innovation Foundation (JCYJ20200109105608771).

Institutional Review Board Statement: Not applicable.

Informed Consent Statement: Not applicable.

Data Availability Statement: Not applicable.

Conflicts of Interest: The authors declare no conflict of interest.

References

1. Day, Y.S.; Baird, C.L.; Rich, R.L.; Myszkowski, D.G. Direct comparison of binding equilibrium, thermodynamic, and rate constants determined by surface- and solution-based biophysical methods. *Protein Sci.* **2002**, *11*, 1017–1025.
2. Wood, R.W. On a remarkable case of uneven distribution of light in a diffraction grating spectrum. *Lond. Edinb. Dublin Philos. Mag. J. Sci.* **2009**, *4*, 396–402.
3. Johnston, S.K.; Mar, M.; Yee, S.S. Prototype of a multi-channel planar substrate spr probe. *Sens. Actuators B Chem.* **1999**, *54*, 57–65.
4. Jansson, M.; Uhlen, M.; Nilsson, B. Structural changes in insulin-like growth factor (igf) i mutant proteins affecting binding kinetic rates to igf binding protein 1 and igf-i receptor. *Biochemistry* **1997**, *36*, 4108–4117.
5. Carrascosa, L.G.; Sina, A.A.; Palanisamy, R.; Sepulveda, B.; Otte, M.A.; Rauf, S.; Shiddiky, M.J.; Trau, M. Molecular inversion probe-based spr biosensing for specific, label-free and real-time detection of regional DNA methylation. *Chem. Commun.* **2014**, *50*, 3585–3588.
6. Pollet, J.; Delpont, F.; Janssen, K.P.; Jans, K.; Maes, G.; Pfeiffer, H.; Wevers, M.; Lammertyn, J. Fiber optic spr biosensing of DNA hybridization and DNA-protein interactions. *Biosens. Bioelectron.* **2009**, *25*, 864–869.
7. Zhang, F.; Wang, S.; Yin, L.; Yang, Y.; Guan, Y.; Wang, W.; Xu, H.; Tao, N. Quantification of epidermal growth factor receptor expression level and binding kinetics on cell surfaces by surface plasmon resonance imaging. *Anal. Chem.* **2015**, *87*, 9960–9965.
8. Campbell, C.T.; Kim, G. Spr microscopy and its applications to high-throughput analyses of biomolecular binding events and their kinetics. *Biomaterials* **2007**, *28*, 2380–2392.
9. Fasoli, J.B.; Corn, R.M. Surface enzyme chemistries for ultrasensitive microarray biosensing with spr imaging. *Langmuir* **2015**, *31*, 9527–9536.
10. Hinman, S.S.; Ruiz, C.J.; Drakakaki, G.; Wilkop, T.E.; Cheng, Q. On-demand formation of supported lipid membrane arrays by trehalose-assisted vesicle delivery for spr imaging. *ACS Appl Mater. Interfaces* **2015**, *7*, 17122–17130.
11. Manuel, G.; Luptak, A.; Corn, R.M. A microwell-printing fabrication strategy for the on-chip templated biosynthesis of protein microarrays for surface plasmon resonance imaging. *J. Phys. Chem. C Nanomater. Interfaces* **2016**, *120*, 20984–20990.
12. Scarano, S.; Mascini, M.; Turner, A.P.; Minunni, M. Surface plasmon resonance imaging for affinity-based biosensors. *Biosens. Bioelectron.* **2010**, *25*, 957–966.
13. Giebel, K.F.; Bechinger, C.; Herminghaus, S.; Riedel, M.; Leiderer, P.; Weiland, U.; Bastmeyer, M. Imaging of cell/substrate contacts of living cells with surface plasmon resonance microscopy. *Biophys. J.* **1999**, *76*, 509–516.
14. Huang, B.; Yu, F.; Zare, R.N. Surface plasmon resonance imaging using a high numerical aperture microscope objective. *Anal. Chem.* **2007**, *79*, 2979–2983.
15. Smith, E.A.; Corn, R.M. Surface plasmon resonance imaging as a tool to monitor biomolecular interactions in an array based format. *Appl. Spectrosc.* **2003**, *57*, 320A–332A.

16. Wang, D.; Loo, J.F.C.; Chen, J.; Yam, Y.; Chen, S.C.; He, H.; Kong, S.K.; Ho, H.P. Recent advances in surface plasmon resonance imaging sensors. *Sensors* **2019**, *19*, 1266.
17. Kretschmann, E.; Raether, H. Notizen: Radiative decay of non radiative surface plasmons excited by light. *Z. Für. Nat. A* **1968**, *23*, 2135–2136.
18. Yu, H.; Shan, X.; Wang, S.; Chen, H.; Tao, N. Molecular scale origin of surface plasmon resonance biosensors. *Anal. Chem.* **2014**, *86*, 8992–8997.
19. Kano, H.; Knoll, W. Locally excited surface-plasmon-polaritons for thickness measurement of lbc films. *Opt. Commun.* **1998**, *153*, 235–239.
20. Somekh, M.G.; Liu, S.G.; Velinov, T.S.; See, C.W. Optical $v(z)$ for high-resolution 2π surface plasmon microscopy. *Opt. Lett.* **2000**, *25*, 823–825.
21. Zhang, B.; Pechprasarn, S.; Zhang, J.; Somekh, M.G. Confocal surface plasmon microscopy with pupil function engineering. *Opt. Express* **2012**, *20*, 7388–7397.
22. Watanabe, K.; Miyazaki, R.; Terakado, G.; Okazaki, T.; Morigaki, K.; Kano, H. High resolution imaging of patterned model biological membranes by localized surface plasmon microscopy. *Appl. Opt.* **2010**, *49*, 887–891.
23. Kuai, Y.; Chen, J.; Tang, X.; Xiang, Y.; Lu, F.; Kuang, C.; Xu, L.; Shen, W.; Cheng, J.; Gui, H.; et al. Label-free surface-sensitive photonic microscopy with high spatial resolution using azimuthal rotation illumination. *Sci. Adv.* **2019**, *5*, eaav5335.
24. Chen, Y.; Zhang, D.; Han, L.; Rui, G.; Wang, X.; Wang, P.; Ming, H. Surface-plasmon-coupled emission microscopy with a polarization converter. *Opt. Lett.* **2013**, *38*, 736–738.
25. Son, T.; Lee, C.; Seo, J.; Choi, I.H.; Kim, D. Surface plasmon microscopy by spatial light switching for label-free imaging with enhanced resolution. *Opt. Lett.* **2018**, *43*, 959–962.
26. Son, T.; Lee, C.; Moon, G.; Lee, D.; Cheong, E.; Kim, D. Enhanced surface plasmon microscopy based on multi-channel spatial light switching for label-free neuronal imaging. *Biosens. Bioelectron.* **2019**, *146*, 111738.
27. Yu, H.; Shan, X.; Wang, S.; Tao, N. Achieving high spatial resolution surface plasmon resonance microscopy with image reconstruction. *Anal. Chem.* **2017**, *89*, 2704–2707.
28. Yang, Y.; Shen, G.; Wang, H.; Li, H.; Zhang, T.; Tao, N.; Ding, X.; Yu, H. Interferometric plasmonic imaging and detection of single exosomes. *Proc. Natl. Acad. Sci. USA* **2018**, *115*, 10275–10280.
29. Yang, Y.; Yu, H.; Shan, X.; Wang, W.; Liu, X.; Wang, S.; Tao, N. Label-free tracking of single organelle transportation in cells with nanometer precision using a plasmonic imaging technique. *Small* **2015**, *11*, 2878–2884.
30. Shan, X.; Fang, Y.; Wang, S.; Guan, Y.; Chen, H.Y.; Tao, N. Detection of charges and molecules with self-assembled nano-oscillators. *Nano Lett.* **2014**, *14*, 4151–4157.
31. Wang, W.; Wang, S.; Liu, Q.; Wu, J.; Tao, N. Mapping single-cell-substrate interactions by surface plasmon resonance microscopy. *Langmuir* **2012**, *28*, 13373–13379.
32. Zeng, Y.; Zhou, J.; Wang, X.; Cai, Z.; Shao, Y. Wavelength-scanning surface plasmon resonance microscopy: A novel tool for real time sensing of cell-substrate interactions. *Biosens. Bioelectron.* **2019**, *145*, 111717.
33. Zhang, J.; Dai, S.; Ma, C.; Di, J.; Zhao, J. Common-path digital holographic microscopy for near-field phase imaging based on surface plasmon resonance. *Appl. Opt.* **2017**, *56*, 3223–3228.
34. Dou, J.; Dai, S.; Dong, C.; Zhang, J.; Di, J.; Zhao, J. Dual-channel illumination surface plasmon resonance holographic microscopy for resolution improvement. *Opt. Lett.* **2021**, *46*, 1604–1607.
35. Yang, C.T.; Mejjard, R.; Griesser, H.J.; Bagnaninchi, P.O.; Thierry, B. Cellular micromotion monitored by long-range surface plasmon resonance with optical fluctuation analysis. *Anal. Chem.* **2015**, *87*, 1456–1461.
36. Wang, W.; Yang, Y.; Wang, S.; Nagaraj, V.J.; Liu, Q.; Wu, J.; Tao, N. Label-free measuring and mapping of binding kinetics of membrane proteins in single living cells. *Nat. Chem.* **2012**, *4*, 846–853.
37. Wang, S.; Shan, X.; Patel, U.; Huang, X.; Lu, J.; Li, J.; Tao, N. Label-free imaging, detection, and mass measurement of single viruses by surface plasmon resonance. *Proc. Natl. Acad. Sci. USA* **2010**, *107*, 16028–16032.
38. Syal, K.; Iriya, R.; Yang, Y.; Yu, H.; Wang, S.; Haydel, S.E.; Chen, H.Y.; Tao, N. Antimicrobial susceptibility test with plasmonic imaging and tracking of single bacterial motions on nanometer scale. *ACS Nano* **2016**, *10*, 845–852.
39. Yu, H.; Shan, X.; Wang, S.; Chen, H.; Tao, N. Plasmonic imaging and detection of single DNA molecules. *ACS Nano* **2014**, *8*, 3427–3433.
40. Tan, H.M.; Pechprasarn, S.; Zhang, J.; Pitter, M.C.; Somekh, M.G. High resolution quantitative angle-scanning widefield surface plasmon microscopy. *Sci. Rep.* **2016**, *6*, 20195.
41. Halpern, A.R.; Wood, J.B.; Wang, Y.; Corn, R.M. Single-nanoparticle near-infrared surface plasmon resonance microscopy for real-time measurements of DNA hybridization adsorption. *ACS Nano* **2014**, *8*, 1022–1030.
42. Foley, K.J.; Shan, X.; Tao, N.J. Surface impedance imaging technique. *Anal. Chem.* **2008**, *80*, 5146–5151.
43. MacGriff, C.; Wang, S.; Wiktor, P.; Wang, W.; Shan, X.; Tao, N. Charge-based detection of small molecules by plasmonic-based electrochemical impedance microscopy. *Anal. Chem.* **2013**, *85*, 6682–6687.
44. Zhang, P.; Ma, G.; Dong, W.; Wan, Z.; Wang, S.; Tao, N. Plasmonic scattering imaging of single proteins and binding kinetics. *Nat. Methods* **2020**, *17*, 1010–1017.
45. Zhang, P.; Ma, G.; Wan, Z.; Wang, S. Quantification of single-molecule protein binding kinetics in complex media with prism-coupled plasmonic scattering imaging. *ACS Sens.* **2021**, *6*, 1357–1366.

46. Chen, Z.; Peng, Y.; Cao, Y.; Wang, H.; Zhang, J.R.; Chen, H.Y.; Zhu, J.J. Light-driven nano-oscillators for label-free single-molecule monitoring of microRNA. *Nano Lett.* **2018**, *18*, 3759–3765.
47. Ma, G.; Wan, Z.; Yang, Y.; Zhang, P.; Wang, S.; Tao, N. Optical imaging of single-protein size, charge, mobility, and binding. *Nat. Commun.* **2020**, *11*, 4768.
48. Moon, G.; Son, T.; Lee, H.; Kim, D. Deep learning approach for enhanced detection of surface plasmon scattering. *Anal. Chem.* **2019**, *91*, 9538–9545.
49. Wang, X.; Zeng, Q.; Xie, F.; Wang, J.; Yang, Y.; Xu, Y.; Li, J.; Yu, H. Automated nanoparticle analysis in surface plasmon resonance microscopy. *Anal. Chem.* **2021**, *93*, 7399–7404.
50. Chen, J.; Zeng, Y.; Zhou, J.; Wang, X.; Jia, B.; Miyan, R.; Zhang, T.; Sang, W.; Wang, Y.; Qiu, H.; et al. Optothermophoretic flipping method for biomolecule interaction enhancement. *Biosens. Bioelectron.* **2022**, *204*, 114084.
51. Liu, S.; Lin, L.; Sun, H.B. Opto-thermophoretic manipulation. *ACS Nano* **2021**, *15*, 5925–5943.
52. Chen, J.; Kang, Z.; Kong, S.K.; Ho, H.P. Plasmonic random nanostructures on fiber tip for trapping live cells and colloidal particles. *Opt. Lett.* **2015**, *40*, 3926–3929.
53. Dai, S.; Mi, J.; Dou, J.; Lu, H.; Dong, C.; Ren, L.; Zhao, R.; Shi, W.; Zhang, N.; Zhou, Y.; et al. Optical tweezers integrated surface plasmon resonance holographic microscopy for characterizing cell-substrate interactions under noninvasive optical force stimuli. *Biosens. Bioelectron.* **2022**, *206*, 114131.
54. Zhou, J.; Dai, X.; Jia, B.; Qu, J.; Ho, H.-P.; Gao, B.Z.; Shao, Y.; Chen, J. Nanorefrigerative tweezers for optofluidic manipulation. *Appl. Phys. Lett.* **2022**, *120*, 163701.
55. Tan, P.S.; Yuan, X.C.; Lin, J.; Wang, Q.; Mei, T.; Burge, R.E.; Mu, G.G. Surface plasmon polaritons generated by optical vortex beams. *Appl. Phys. Lett.* **2008**, *92*, 111108.
56. Moh, K.J.; Yuan, X.C.; Bu, J.; Zhu, S.W.; Gao, B.Z. Surface plasmon resonance imaging of cell-substrate contacts with radially polarized beams. *Opt. Express* **2008**, *16*, 20734–20741.
57. Shen, J.; Wang, J.; Zhang, C.; Min, C.; Fang, H.; Du, L.; Zhu, S.; Yuan, X.C. Dynamic plasmonic tweezers enabled single-particle-film-system gap-mode surface-enhanced Raman scattering. *Appl. Phys. Lett.* **2013**, *103*, 191119.
58. Dou, X.; Yang, A.; Min, C.; Du, L.; Zhang, Y.; Weng, X.; Yuan, X. Polarization-controlled gap-mode surface-enhanced Raman scattering with a single nanoparticle. *J. Phys. D Appl. Phys.* **2017**, *50*, 255302.
59. Hu, Z.J.; Yuan, X.C.; Zhu, S.W.; Yuan, G.H.; Tan, P.S.; Lin, J.; Wang, Q. Dynamic surface plasmon patterns generated by reconfigurable “cogwheel-shaped” beams. *Appl. Phys. Lett.* **2008**, *93*, 181102.
60. Man, Z.; Du, L.; Min, C.; Zhang, Y.; Zhang, C.; Zhu, S.; Paul Urbach, H.; Yuan, X.C. Dynamic plasmonic beam shaping by vector beams with arbitrary locally linear polarization states. *Appl. Phys. Lett.* **2014**, *105*, 011110.
61. Jia, B.; Chen, J.; Zhou, J.; Zeng, Y.; Ho, H.-P.; Shao, Y. Passively and actively enhanced surface plasmon resonance sensing strategies towards single molecular detection. *Nano Res.* **2022**, *15*, 8367–8388.